

A clumpy and anisotropic galaxy halo at $z=1$ from gravitational-arc tomography

Sebastian Lopez^{1,*}, Nicolas Tejos², Cédric Ledoux³, L. Felipe Barrientos⁴, Keren Sharon⁵, Jane R. Rigby⁶, Michael D. Gladders^{7,8}, Matthew B. Bayliss⁹, & Ismael Pessa⁴

¹*Departamento de Astronomía, Universidad de Chile, Casilla 36-D, Santiago, Chile; *slopez@das.uchile.cl*

²*Instituto de Física, Pontificia Universidad Católica de Valparaíso, Casilla 4059, Valparaíso, Chile*

³*European Southern Observatory, Alonso de Córdova 3107, Casilla 19001, Vitacura, 19, Santiago, Chile*

⁴*Instituto de Astrofísica, Pontificia Universidad Católica de Chile, Vicuña Mackenna 4860, Santiago, Chile*

⁵*Department of Astronomy, University of Michigan, 500 Church St., Ann Arbor, MI 48109, USA*

⁶*Observational Cosmology Lab, NASA Goddard Space Flight Center, 8800 Greenbelt Rd., Greenbelt, MD 20771, USA*

⁷*Department of Astronomy & Astrophysics, University of Chicago, 5640 S. Ellis Ave., Chicago, IL 60637, USA*

⁸*Kavli Institute for Cosmological Physics, University of Chicago, 5640 S. Ellis Ave., Chicago, IL 60637, USA*

⁹*Kavli Institute for Astrophysics & Space Research, Massachusetts Institute of Technology, 77 Massachusetts Avenue, Cambridge, MA 02139, USA*

Every star-forming galaxy has a halo of metal-enriched gas extending out to at least 100 kpc¹⁻³, as revealed by the absorption lines this gas imprints on the spectra of background quasars⁴. However, quasars are sparse and typically probe only one narrow pencil beam through the intervening galaxy. Close quasar pairs⁵⁻⁷ and gravitationally lensed quasars⁸⁻¹¹ have been used to circumvent this inherently one-dimensional technique, but these objects are rare and the structure of the circum-galactic medium remains poorly constrained. As a result, our understanding of the physical processes that drive the re-cycling of baryons across the lifetime of a galaxy is limited^{12,13}. Here we report integral-field (tomographic) spectroscopy of an extended background source—a bright giant gravitational arc. We can thus coherently map the spatial and kinematic distribution of Mg II absorption—a standard tracer of enriched gas—in an intervening galaxy system at redshift 0.98 (i.e., ~ 8 Gyr ago). Our gravitational-arc tomography unveils a clumpy medium in which the absorption-strength decreases with increasing impact parameter, in good agreement with the statistics towards quasars; furthermore, we find strong evidence that the gas is not distributed isotropically. Interestingly, we detect little kinematic variation over a projected area of ≈ 600 kpc², with all line-of-sight velocities confined to within a few tens of km s⁻¹ of each other. These results suggest that the detected absorption originates from entrained recycled material, rather than in a galactic outflow.

We use the Multi Unit Spectroscopic Explorer (MUSE)¹⁴ mounted on the European Southern Observatory Very Large Telescope to observe the 38'' long gravitational arc RCSGA 032727–132623¹⁵. This arc results from a lensed galaxy at redshift 1.70, highly magnified and stretched by a massive galaxy cluster at redshift 0.56 (Figure 1). With $g = 19.15$, it is among the brightest known arcs¹⁶ and has a high surface brightness across a large area on the sky¹⁷. Magellan/MagE spectroscopy¹⁸ of its brightest knot reveals the presence of a strong Mg II absorption system at redshift $z_{\text{abs}} = 0.98$, and we set out to map this absorption along the entire arc.

Figure 2 shows a MUSE map of $z_{\text{abs}} = 0.98$ Mg II absorption-strength at different positions along RCSGA 032727–132623. The arc positions span impact parameters—in the absorber plane; see Methods—of ≈ 15 –90 kpc to the absorbing galaxy system (hereafter “G1”), indicated by the blue circle. G1 is our primary candidate absorber (out of three [O II] detections at redshift 0.98, namely G1, G2, and G3; Methods) and deserves special attention. *HST* continuum images resolve this system into three irregular galaxies, hereafter G1-A, G1-B and G1-C, all having blue $B - I$ colors. From the *HST* photometry we estimate these galaxies to have low luminosities, $\lesssim 0.05 L^*$, and consequently also low stellar masses, compared to quasar absorbers³. Such stellar masses suggest total halo masses of $\sim 10^{11} M_{\odot}$, which in turn define their virial radii to be $R_{\text{vir}} \sim 90$ kpc (Methods). Additionally, from the [O II] $\lambda\lambda 3726, 3729$ emission doublets, we estimate their star-formation rates to amount to $\lesssim 0.2 M_{\odot} \text{ yr}^{-1}$. We use the [O II] velocities to define a “systemic” redshift at $z_{\text{G1}} = 0.98235$.

Four key features are readily evident from Figure 2: (a) Mg II is detected from ≈ 15 out to ≈ 45 kpc to the South of G1 but not detected further than ≈ 80 kpc to the West (another arc knot in the South—not shown in the Figure—also has sensitive non-detections; see below); (b) the absorption-strength is not uniform, indicating a clumpy medium on 4 kpc scales down to our detection limit of $\approx 0.4 \text{ \AA}$; (c) the line centroids vary little (within one spectral pixel, or $\sim 50 \text{ km s}^{-1}$) all across the arc; and (d) most of the doublet ratios appear to be saturated, indicating possible partial covering of the background source (Methods).

Figure 3 shows that the absorption-strength decreases with impact parameter, in broad agreement with the quasar statistics³, but the scatter is *smaller* than in the quasar data^{2,3}. The latter is likely a consequence of partial covering, which would skew down the arc measurements (Methods); however, the heterogeneity of the compiled quasar-galaxy sample may also play a role^{3,19}, as the intervening galaxies encompass a wide range of masses, luminosities, and orientations. That is to say, we compare averages over different areas in a single galaxy (probed by the arc) with an average over many distinct galaxies (probed by quasars).

From quasar lens statistics^{8,20}, we know transverse structure is detected on similar scales as probed by our 4 kpc, seeing-limited resolution, and below. This indicates that the metals traced by Mg II are concentrated in small clouds we do not resolve here but are spatially distributed in such a way to produce the gradient we observe. Therefore, the present data do not probe individual cloud sizes but rather their coherence length. Some stringent non-detections (Figure 3) re-enforce the notion of clumpiness on kpc scales.

The present tomographic technique allows us to scan the velocity field of the absorbing gas profusely in a single high-redshift halo¹⁰. Figure 4 displays absorption velocities and emission velocities of G1-A, G1-B and G1-C as a function of impact parameter. The first outstanding feature in this Figure is that all absorption velocities lie to the red of z_{G1} , at $+62 \text{ km s}^{-1}$, although none of them substantially exceeds any of the galaxy velocity dispersions. Secondly, there is little variation

in absorption velocity ($\approx 24 \text{ km s}^{-1}$) overall along the arc, even less than within the galaxy system itself, but extending out to 40 kpc, i.e. 10 times larger distances than the projected separations between the G1 galaxies! Along with a clumpy medium revealed by the map of absorption-strengths, this kinematically *quiet* behavior places strong constraints on the geometry and dynamics of this system.

Assuming saturation, the absorption-strengths are a measure of the velocity spread of individual clouds²¹ (not resolved by our data) and possible partial covering (see Methods). Thus, most of our detections would correspond to velocity spreads $\lesssim 108 \text{ km s}^{-1}$ along the sightlines, the equivalent of a 1 \AA absorption line. Interestingly, we find a lower scatter in the *transverse* direction. Taken together, this would indicate gas clouds whose internal velocity dispersions dominate over bulk motions. For the impact parameters and halo mass probed here, these velocities resemble those determined at higher spectral resolution in low-redshift systems^{22,23}, which appear well within the halo escape velocity and virial radius.

Our observations do not support a spherical geometry^{24,25}. Indeed, the Mg II gas does not seem to be distributed isotropically around G1; if this were the case, similar absorption would occur at both sides of the line connecting G1 and its closest arc position, which we do not see. Instead, there are more non-detections on the Southern side. G2 (Methods) is also a good example of this situation, as no Mg II is detected in six positions at $\approx 20\text{--}30$ kpc to sensitive limits, while 4 are expected if G2 followed the trend shown in Figure 3 isotropically. Furthermore, assuming the observed Mg II to be related to only one of the G1 galaxies, then only one out of four galaxies (including G2) presents detectable absorption, which leads to a rough covering fraction of $\approx 25\%$ within 40 kpc. This interpretation assumes that the G1 galaxies are distinct objects and not part of a large disk of gas and dust (Methods). Thus, in line with quasar-absorber observations^{26,27}, our arc observations strongly suggest that the absorbing gas is anisotropic, showing wide (possibly $\sim 90^\circ$) opening angles²⁸.

Our data also allow us to compute gas covering fractions in an alternative fashion, namely *directly* from our “hits and misses” statistics around G1 only (Methods). Assuming anisotropy, we probe here the preferential G1 direction that shows absorption; therefore, our covering fraction estimate should lie *above* that of quasar absorbers, because those surveys probe random quasar-galaxy orientations. Interestingly enough, our prediction is fulfilled in comparison with *galaxy-selected* quasar absorbers², which we regard to be unbiased: the covering fraction towards the arc is indeed larger than towards the quasars in that sample (Methods). Conversely, a comparison with more heterogeneous samples that include Mg II-*selected* galaxies³ gives smaller covering fractions towards the arc than towards the quasars. This suggests possible selection biases in the latter samples, because by construction they favour galaxy orientations producing absorption¹⁹.

At *low redshift* there is observational evidence^{23,29} that the circum-galactic medium of star-forming galaxies is driven by the interplay between major-axis entraining gas (pristine or re-cycled)

and enriched outflows aligned with the minor axis. Although this picture is also consistent with most recent simulations and Λ CDM predictions³⁰, it remains yet to be confirmed, particularly at high redshift. Here we deal with dwarf galaxies at redshift one, still able to eject metals¹² out to one virial radius, beyond which the metal flux is expected to have decreased markedly³⁰. The present Mg II detections occur well within R_{vir} and therefore could be originating from any of the G1 galaxies (but given the relatively quiet velocity field most probably from only one of them). In addition, the gas is metal-enriched (including Mg II and Fe II; see Methods) and patchy (perhaps revealing a multi-phase medium), which suggests re-cycled gas either outflowing from or bound to one of the individual G1 halos. The outflow scenario requires outflow speeds^{6,26} in excess of the galaxy-gas velocity offsets observed here (Figure 4). This suggests that the Mg II is more likely correlated with entrained gas in the extended halo of G1-B, (closer in velocity) or even G1-A, in which case the absorption velocity offset would resemble the one-sided velocity offsets seen at low redshift^{22,23}.

The novel gravitational-arc tomography presented here appears to probe the gaseous extension of a galaxy halo *in formation*, beyond ≈ 20 kpc scales, which might be a remnant of past gravitational interactions forming tidal debris and gaseous streams infalling back into the overall G1 potential well. Unfortunately, the arc-galaxy configuration under study does not cover lower impact parameters for testing this hypothesis, but future objects may permit more conclusive detections.

References

1. Churchill, C. W. *et al.* Low- and High-Ionization Absorption Properties of Mg II Absorption-selected Galaxies at Intermediate Redshifts. I. General Properties. *Astrophys. J. Suppl. Ser.* **130**, 91–119 (2000).
2. Chen, H.-W. *et al.* An Empirical Characterization of Extended Cool Gas Around Galaxies Using Mg II Absorption Features. *Astrophys. J.* **714**, 1521–1541 (2010).
3. Nielsen, N. M., Churchill, C. W. & Kacprzak, G. G. MAGIICAT II. General Characteristics of the Mg II Absorbing Circumgalactic Medium. *Astrophys. J.* **776**, 115 (2013).
4. Chen, H.-W. Outskirts of Distant Galaxies In Absorption. *ArXiv e-prints* (2016).
5. Tytler, D. *et al.* Metal absorption systems in spectra of pairs of QSOs: how absorbers cluster around QSOs and other absorbers. *Mon. Not. R. Astron. Soc.* **392**, 1539–1572 (2009).
6. Martin, C. L. *et al.* The Size and Origin of Metal-enriched Regions in the Intergalactic Medium from Spectra of Binary Quasars. *Astrophys. J.* **721**, 174–192 (2010).
7. Hennawi, J. F. *et al.* Binary Quasars in the Sloan Digital Sky Survey: Evidence for Excess Clustering on Small Scales. *Astronom. J.* **131**, 1–23 (2006).

8. Rauch, M., Sargent, W. L. W., Barlow, T. A. & Carswell, R. F. Small-Scale Structure at High Redshift. III. The Clumpiness of the Intergalactic Medium on Subkiloparsec Scales. *Astrophys. J.* **562**, 76–87 (2001).
9. Lopez, S., Ellison, S., D’Odorico, S. & Kim, T.-S. Clues to the nature of high-redshift O vi absorption systems from their lack of small-scale structure. *Astron. & Astrophys.* **469**, 61–74 (2007).
10. Chen, H.-W. *et al.* Spatially resolved velocity maps of halo gas around two intermediate-redshift galaxies. *Mon. Not. R. Astron. Soc.* **438**, 1435–1450 (2014).
11. Rubin, K. H. R. *et al.* Andromeda’s Parachute: A Bright Quadruply Lensed Quasar at $z=2.377$. *ArXiv e-prints* (2017).
12. Kereš, D., Katz, N., Weinberg, D. H. & Davé, R. How do galaxies get their gas? *Mon. Not. R. Astron. Soc.* **363**, 2–28 (2005).
13. Muratov, A. L. *et al.* Gusty, gaseous flows of FIRE: galactic winds in cosmological simulations with explicit stellar feedback. *Mon. Not. R. Astron. Soc.* **454**, 2691–2713 (2015).
14. Bacon, R. *et al.* The MUSE second-generation VLT instrument. In *Ground-based and Airborne Instrumentation for Astronomy III*, vol. 7735 of *Proceedings of the SPIE*, 773508 (2010).
15. Wuyts, E. *et al.* A Bright, Spatially Extended Lensed Galaxy at $z = 1.7$ Behind the Cluster RCS2 032727-132623. *Astrophys. J.* **724**, 1182–1192 (2010).
16. Dahle, H. *et al.* Discovery of an exceptionally bright giant arc at $z = 2.369$, gravitationally lensed by the Planck cluster PSZ1 G311.65-18.48. *Astron. & Astrophys.* **590**, L4 (2016).
17. Rigby, J. R., Wuyts, E., Gladders, M. D., Sharon, K. & Becker, G. D. The Physical Conditions of a Lensed Star-forming Galaxy at $z = 1.7$. *Astrophys. J.* **732**, 59 (2011).
18. Rigby J. R. *et al.*, submitted to *Astrophys. J. Suppl. Ser.*.
19. Nielsen, N. M., Churchill, C. W., Kacprzak, G. G. & Murphy, M. T. MAGIICAT I. The Mg II Absorber-Galaxy Catalog. *Astrophys. J.* **776**, 114 (2013).
20. Lopez, S. *et al.* Metal Abundances in a Damped Ly α System along Two Lines of Sight at $z = 0.93$. *Astrophys. J.* **626**, 767–775 (2005).
21. Ellison, S. L. An efficient technique for pre-selecting low-redshift damped Ly α systems. *Mon. Not. R. Astron. Soc.* **368**, 335–340 (2006).
22. Tumlinson, J. *et al.* The COS-Halos Survey: Rationale, Design, and a Census of Circumgalactic Neutral Hydrogen. *Astrophys. J.* **777**, 59 (2013).

23. Ho, S. H., Martin, C. L., Kacprzak, G. G. & Churchill, C. W. Quasars Probing Galaxies. I. Signatures of Gas Accretion at Redshift Approximately 0.2. *Astrophys. J.* **835**, 267 (2017).
24. Steidel, C. C. The Nature and Evolution of Absorption-Selected Galaxies. In Meylan, G. (ed.) *QSO Absorption Lines*, 139 (1995).
25. Charlton, J. C. & Churchill, C. W. MG II Absorbing Galaxies: Halos or Disks? *Astrophys. J.* **465**, 631 (1996).
26. Bouché, N. *et al.* Physical properties of galactic winds using background quasars. *Mon. Not. R. Astron. Soc.* **426**, 801–815 (2012).
27. Kacprzak, G. G., Churchill, C. W. & Nielsen, N. M. Tracing Outflows and Accretion: A Bimodal Azimuthal Dependence of Mg II Absorption. *Astroph. J. Letters* **760**, L7 (2012).
28. Bordoloi, R., Lilly, S. J., Kacprzak, G. G. & Churchill, C. W. Modeling the Distribution of Mg II Absorbers around Galaxies Using Background Galaxies and Quasars. *Astrophys. J.* **784**, 108 (2014).
29. Kacprzak, G. G. Gas Accretion in Star-Forming Galaxies. In Fox, A. & Davé, R. (eds.) *Astrophysics and Space Science Library*, vol. 430 of *Astrophysics and Space Science Library*, 145 (2017).
30. Muratov, A. L. *et al.* Metal flows of the circumgalactic medium, and the metal budget in galactic haloes. *Mon. Not. R. Astron. Soc.* **468**, 4170–4188 (2017).

Acknowledgements This work has benefitted from discussions with Alain Smette, Nicole Nielsen and Glenn Kacprzak. S.L. thanks the European Southern Observatory Scientific Visitor Selection Committee for supporting a research stay at the ESO headquarters in Santiago, where part of this work was done. S.L. has been supported by FONDECYT grant number 1140838. This work has also been partially supported by PFB-06 CATA. N.T. acknowledges support from *CONICYT PAI/82140055*.

Author contributions S.L. conceived and led the project. S.L. and N.T. wrote the MUSE telescope-time proposal and designed the observations. L.F.B. and N.T. prepared the remote observations and L.F.B. reduced the MUSE data. S.L., N.T. and C.L. analysed the data, performed simulations, and devised original ways to produce and interpret the results. S.L. wrote the main codes. N.T. and I.P. performed the blind survey of galaxies in the field of view. K.S. performed the lens model and L.F.B. supervised the design of Fig. 1. M.B.B. and L.F.B., performed the photometric characterization of the absorbing galaxies, and S.L., C.L. and N.T. the analysis of their spectra. Ancillary data from MagE and HST were provided by J.R.R. and M.D.G. S.L. wrote the manuscript and crafted the rest of the figures, with contribution from N.T. All co-authors provided critical feedback and helped shape the manuscript.

Competing Interests The authors declare that they have no competing financial interests.

Correspondence Correspondence and requests for materials should be addressed to S. Lopez (email: slopez@das.uchile.cl).

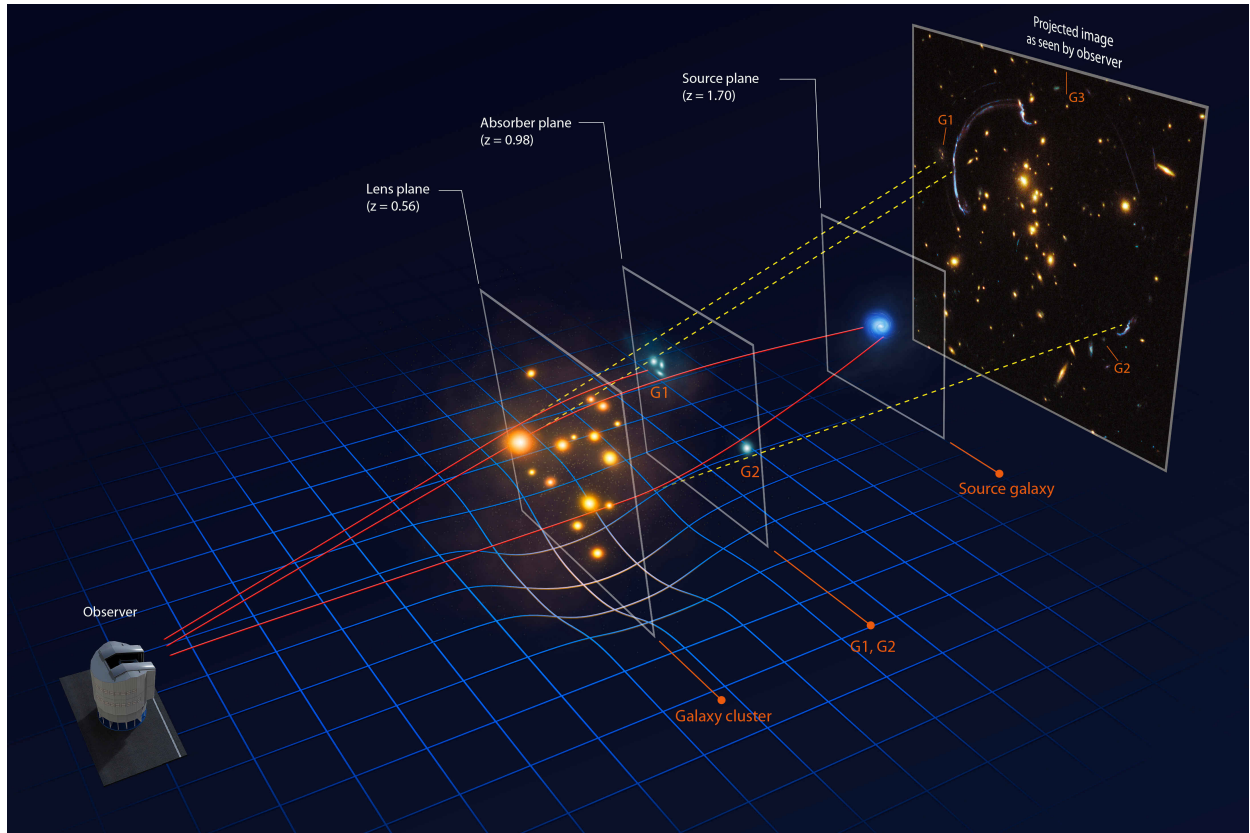


Figure 1: **Illustration of the lens geometry of arc and absorber in RCSGA 032727–132623.** Light from the $z = 1.70$ background galaxy ('source plane') is deflected and magnified by an intervening galaxy cluster at $z = 0.56$ ¹⁵ ('lens plane'), to form the bright giant arc that is seen in the 'image plane' (right-most panel). As the light crosses the $z_{\text{abs}} = 0.98$ absorber plane, some of it is absorbed by Mg II in the gas that surrounds an absorbing galaxy lying close in projection. Three candidates for such galaxies are detected at this redshift, marked 'G1', 'G2' and 'G3' in the image plane. The present work deals with G1 and G2 (indicated also in the absorber plane), which probe the closest projected distances to the arc. (Image produced by Carlos Polanco).

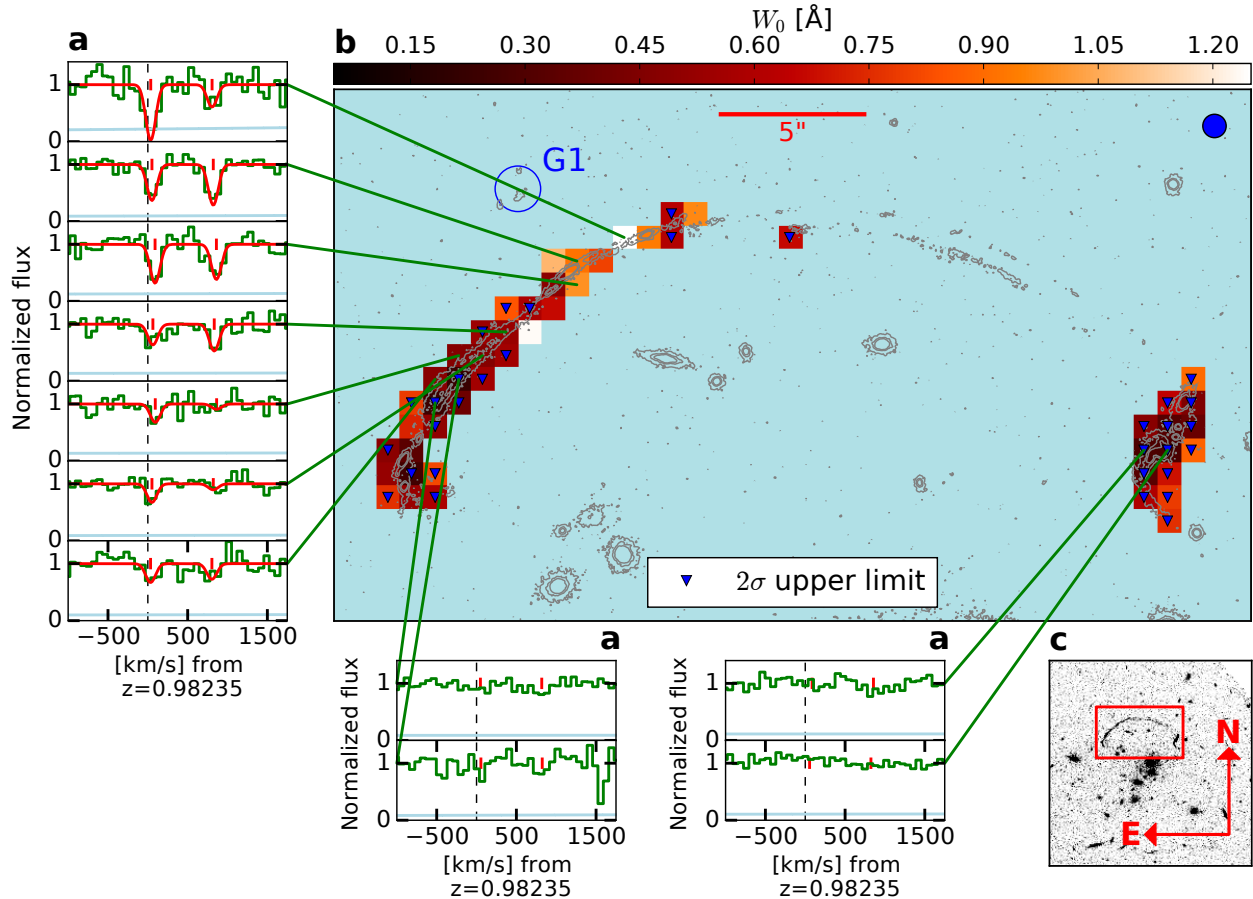


Figure 2: **Map of Mg II absorption-strengths at ≈ 4 kpc resolution.** (a): Representative sample of Mg II $\lambda\lambda 2796, 2803$ MUSE spectra (green histograms) and corresponding Gaussian fits (red lines) in velocity space with respect to $z_{G1} = 0.98235$. Panels without fits correspond to non-detections. The green lines indicate the corresponding positions on the arc. (b): $0.51' \times 0.27'$ inset of the $1' \times 1'$ MUSE field centered in the north-eastern part of the arc. The color scale indicates Mg II $\lambda 2796$ rest-frame absorption-strengths obtained from the Gaussian fits. A total of 56 positions were selected to have a continuum signal-to-noise ratio $S/N > 3$ at the expected Mg II lines (50 shown here), out of which 18 have significant detections (see Methods). Non-detections are indicated by blue downward arrows in the map. The candidate absorber, G1, is indicated by the blue circumference (to the North-East). For reference, we overlay arc and galaxy contours at 840 nm from *Hubble Space Telescope* (HST) data (GO program 12267; PI: Rigby). Each independent spatial element ('spaxel') is $0.8''$ wide, equivalent to 4 MUSE unbinned spaxels and matching the seeing (indicated by the blue circle on the top-right). This grid is defined in the image plane; the actual spatial resolution varies across the absorber plane from ≈ 4 kpc, at the eastern side of the arc, to ≈ 2 kpc, at the western side. Likewise, the $5''$ scalebar corresponds to a range of ≈ 24 – 12 kpc in the absorber plane, depending on position (for a de-lensed image see Extended Data Figure 3). (c): Entire MUSE field-of-view indicating the location of the Mg II map shown in (b).

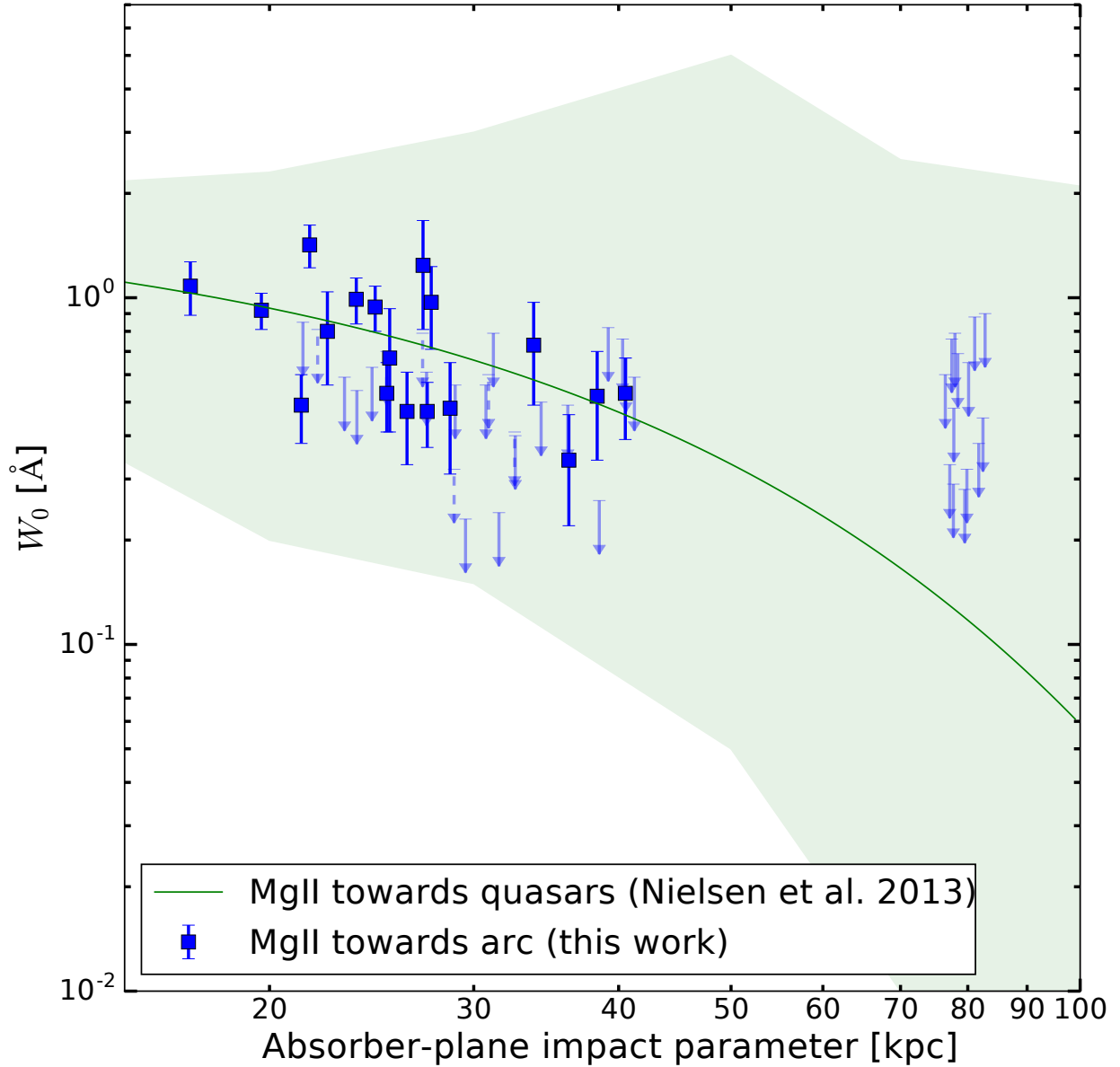


Figure 3: **Arc Mg II absorption-strength versus impact parameter.** Squares correspond to detections and arrows to 2σ upper limits. Error bars correspond to the $\pm 1\sigma$ uncertainty in the W_0 measurement. All impact parameters are measured to G1 (North-East part of the arc), except for the six upper limits marked with dashed lines which correspond to G2 (South). The zero-points are given by the centers of the blue circles in Figure 2 and Extended Data Figure 2. The green line is the fit to a sample of 182 quasar absorption systems³ and the shaded area indicates the full scatter in that sample. Error bars correspond to the $\pm 1\sigma$ uncertainty in the W_0 measurement. Uncertainties in the impact parameters are $\lesssim 5\%$.

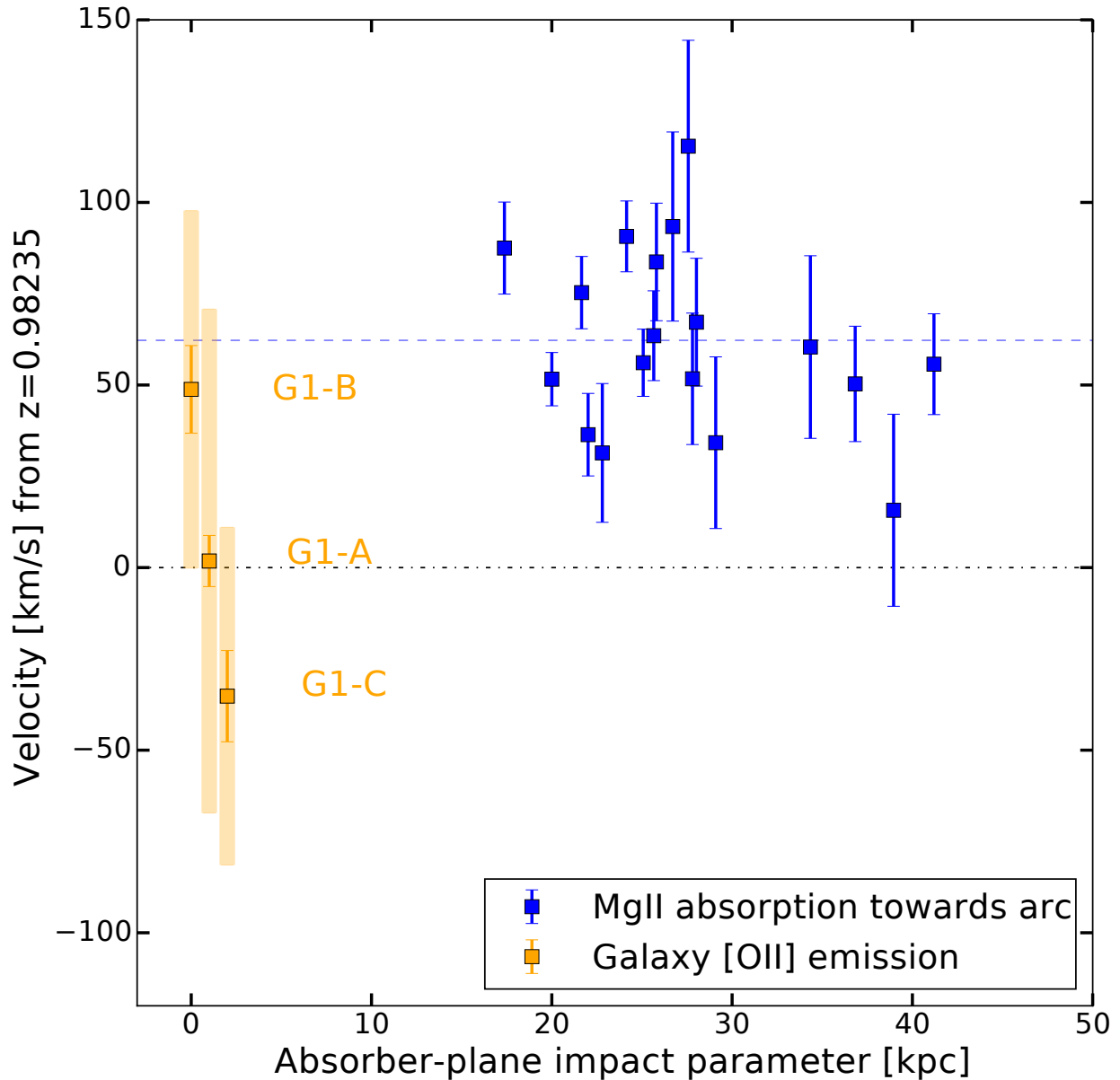


Figure 4: **Gas kinematics.** Blue symbols correspond to arc $\text{Mg II } \lambda\lambda 2796, 2803$ absorption-line velocities; orange symbols to galaxy $[\text{O II}] \lambda\lambda 3726, 3729$ emission line velocities (shifted in the x-axis for clarity). The blue dashed line indicates the average absorption velocity. The zero-point velocity corresponds to the systemic redshift at $z_{\text{G1}} = 0.98235$. Error bars correspond to the $\pm 1\sigma$ uncertainty in the velocities. The envelopes around the emission-line measurements indicate the FWHM velocity dispersion derived from the $[\text{O II}]$ fits. Uncertainties in the impact parameters are $\lesssim 5\%$.

Methods

1 Observations and data reduction.

The data were obtained with the MUSE integral-field spectrograph¹⁴ mounted on the ESO Very Large Telescope. The $1'$ field-of-view is sampled with 349×352 $0.2''$ wide spaxels. MUSE uses image slicers combined with an array of 24 identical spectrographs that provide nearly 100 000 spectra simultaneously. Our setup provided a wavelength range from 4 650 to 9 300 Å at a resolving power $R = \lambda/\Delta\lambda$ ranging from 2 000 to 4 000. Each spectral bin is 1.25 Å wide. The observations were carried out in 'service mode' during dark time, with thin cirrus or clear-sky conditions, airmass below 1.8, and seeing better than $0.8''$. We obtained a total of 21 exposures of 700s on-target each. The exposures were taken within "Observing Blocks" of 4 exposures each. We applied a small dithering and 90° rotations between exposures to reject cosmic rays and minimize patterns of the slicers on the processed combined cube. We reduced all the observations using the MUSE pipeline recipe v1.6.4 and ESO reflex v2.8.5. We analyzed the quality of the individual exposures by measuring the seeing and transparency in the "white" images. Due to changes in the weather conditions during integrations some of the exposures come from aborted observing blocks (but are otherwise 700s long). We discarded 5 of them for having guiding errors, poor PSF, or obvious transparency problems. The remaining 16 exposures were combined into one final science datacube. The total on-target time was therefore 3.1 hours. The sky subtraction was improved on this cube using the Zurich Atmospheric Purge (ZAP) algorithm³¹. The wavelength solution, corrected for the motion of the Earth around the Sun and converted to vacuum, was checked satisfactorily at the position of the arc's brightest knot against our MagE spectrum¹⁸. The spectral resolution at the Mg II absorption lines is $\text{FWHM} = 2.7 \text{ \AA}$ corresponding to $\approx 140 \text{ km s}^{-1}$ (or $R = 2\,100$).

In this work we adopt a flat Λ CDM cosmology with $\Omega_\Lambda = 0.7$, $\Omega_m = 0.3$, and $H_0 = 70 \text{ km s}^{-1} \text{ Mpc}^{-1}$.

2 Spaxel combination.

Unlike quasars, the present source is (a) extended and (b) inhomogeneous in flux given the resolved background galaxy and the inhomogeneous lensing magnifications (Extended Data Figure 1). Therefore, the spectrum extraction must proceed using an ad-hoc flux combination to assure independent flux measurements while maximizing the final S/N per spectral pixel. To first approximation we tried polygons of constant S/N ³⁴ but decided not to use them given that widely different areas complicate the interpretation of absorption against an extended source. Instead, we perform a 'minimum-size' binning based on a fixed grid that was defined by the spatial sampling. Since the seeing profile is sampled with four $0.2''$ spaxels (FWHM) we use 4×4 binning. This means that the center of each binned spaxel lies at least one seeing FWHM from each other. Offsetting the grid by ± 1 unbinned spaxel shows that the choice of zero-point does not affect the results of the present analysis.

3 Spectral extraction.

To extract individual 1-D spectra for each binned spaxel (or “positions”) we applied weights given by $w_{ij} = f_{ij}/v_{ij}$, where f_{ij} and v_{ij} are respectively the calibrated object flux and variance of spaxel (i, j) . This weight is a modified version of that used to optimally combine spectra of different S/N³⁵; it assumes a low detector read-out noise, in which case v_{ij} approximates to the total number of counts. We note that this gives higher weights to brighter spaxels and may introduce a complicated bias towards highly magnified spaxels. Since we were interested in a small spectral range we defined a ‘sub-cube’ containing wavelengths between 5 100 and 6 000 Å. This range includes the Mg II doublet and the transitions Fe II λ 2382, Fe II λ 2600, and Mg I λ 2852 at $z_{\text{abs}} = 0.98$. Since the array of variances is noisy in the spectral direction as well, to avoid introducing noise carried by the spectral weights, we chose a weight integrated in the spectral direction in a small featureless region bluewards of the Mg II lines (the red side is compromised by a sky emission line residual). Also, this weight does not penalize the absorption troughs.

4 Spaxel selection and Gaussian fits

To search for Mg II we first created a S/N map by selecting binned spaxels on top of the arc and having $S/N > 3$ to the blue of the expected Mg II absorption. This selected a total of 56 positions, corresponding to a total projected area surveyed of $\approx 600 \text{ kpc}^2$. At each selected position a spectrum was extracted and an automatic Gaussian fit applied to the spectral region corresponding to $z_{\text{G1}} = 0.98235$. The Mg II λ 2796, 2803 doublet was fitted with two Gaussians having a tied wavelength ratio, free doublet ratio and fixed line width (corresponding to the instrument spectral resolution, $\text{FWHM} = 2.7 \text{ \AA}$). Each fit provides a rest-frame absorption-strength (rest-frame equivalent width or hereafter “ W_0 ”) and a redshift (radial velocity, hereafter “ v ”), along with their statistical errors (Extended Data Tables 1 and 2). Fixing the line width provides more robust fits, as expected, avoiding false positives in low S/N regions. It also assumes the instrumental profile dominates the line profile. This may not hold for all the positions, in which case we estimate a systematic error of $\approx 0.05 \text{ \AA}$ would be introduced in W_0 (not included in the tables).

In addition to the fits, synthetic line-profiles were created for comparison with the data. When a fit failed or the significance was below 3σ , a 2σ upper limit was calculated using the formula $\sigma_{W_0}(1+z) = \text{FWHM}/\langle S/N \rangle$, where σ_{W_0} is the expected rest-frame 1σ error in the W_0 measurement and $\langle S/N \rangle$ the average continuum S/N near the line. The procedure delivers a total of 18 significant Mg II detections, all of them to the North-East of the arc. Finally, to create the absorption-strength and velocity maps the fit W_0 and v values (or the W_0 upper limits) were recorded in images having the same spatial sampling as the S/N map.

We attempted simultaneous fits to Fe II λ 2382 and Mg I λ 2852 tied to the Mg II redshifts (unfortunately, the Fe II λ 2600 transition is blended with the [C III] λ 1907, 1909 emission line doublet from the source galaxy³⁶ and therefore it could not be fitted). We detect significant Fe II at only three positions along the arc (Extended Data Table 3). These positions also show the strongest *and* most significant Mg II absorption. The corresponding Fe II/Mg II strength ratios lie in the

rather narrow range 0.5–0.7 and conform to the quasar statistics of *very strong* ($W_0 > 1 \text{ \AA}$) Mg II systems³⁷. Non-detections do not constrain these ratios at other positions of the arc due to either too weak Mg II or too low S/N. Although the present Fe II data are limited, the similar ratios tentatively hint to homogeneous enrichment along the arc. One of these positions shows a (marginal) Mg I detection.

The absorption signal in the maps, though significant, is expected to be weak and directly affected by the inhomogeneous S/N. To rule out possible artifacts due to reduction or analysis effects, we conducted mock tests by simulating a flat W_0 distribution in a cube having the same S/N per spaxel as the actual data. The outcome of these tests shows that our fitting procedure recovers a true signal in nearly 100% of the (binned) spaxels with $S/N > 3$, which justifies our S/N cutoff.

5 Galaxies at $z = 0.98$

We searched systematically for galaxies in the MUSE cube near $z = 0.98$. The search included continuum sources and emission-line galaxies. We detected a total of 3 [O II] sources, which we refer to as G1, G2 and G3 (Extended Data Figure 2). These form a triangle with sides 42'', 47'' and 64''-long, or $d \approx 231, 259$ and 341 kpc in the absorber plane. G1 is resolved into 3 galaxies in the *HST* continuum images, which are barely resolved by MUSE. We refer to them as G1-A, G1-B and G1-C. From Gaussian fits to the [O II] $\lambda\lambda 3726, 3729$ doublet in the MUSE spectra we obtained redshifts, line velocity dispersions, [O II] luminosities, and star-formation rates for the five galaxies. Note that the deconvolved velocity dispersions are subject to systematics, given the modest MUSE resolution. Assuming virial equilibrium, the velocities of G1, G2 and G3 lead to a virial radius $R_{\text{vir}} < d$ and thus we do not consider them to be bound gravitationally given their projected separations. Instead, we deem them as 3 independent systems that lie in the same large-scale structure at $z = 0.98$.

G1-A, G1-B and G1-C represent our best candidate absorbing galaxy system, due to their proximity to the place where the arc absorption occurs. The close proximity of G1-A, G1-B and G1-C may cast doubts on whether these indeed are distinct galaxies, as opposed to a single disk where dust obscuration would mimic the presence of different objects. The fact that they are resolved also in the rest-frame *I*-band (F160W) supports the existence of distinct galaxies.

We obtained the photometry from *HST* images in the F606W, F814W, F098M, F125W and F160W bands. We used SExtractor³⁸ in dual mode using the detections in the F160W band as reference to obtain AB magnitudes in a 0.8''-diameter aperture. $(B - I)$ rest-frame colors were computed from F814W and F160W given these filters are the closest in effective wavelength. We used a local Scd galaxy spectral template³⁹ that represents well the color of these galaxies, to correct for any mismatch in the effective pass-bands. Small extinction corrections⁴⁰ were also applied. Using the multi-band photometry and a SED fitting code⁴² we estimated luminosities, stellar masses and star-formation rates. These quantities are subject to large uncertainties due to the use of just 5 pass-bands. We also computed star-formation rates for each galaxy from the [O II] line fluxes, integrated

over 16 unbinned spaxels. These line fluxes are subject to extinction and therefore they must be treated as lower limits only. Using Kennicutt’s prescription⁴¹ the emission-line luminosities translate into star-formation rates that are broadly consistent with those obtained from the SED fitting. These values were corrected by magnification μ using our lens model. From the stellar masses we estimate dark-matter halo masses, M_h , using the prediction from abundance-matching⁴³. We then determine the corresponding virial radius using the relation $R_{\text{vir}} = (3M_h/200\rho_c4\pi)^{1/3}$, where ρ_c is the critical density of the Universe at $z = 0.98$. The galaxy data are summarized in Extended Data Table 4.

6 Lens model

We base our lens model on a previous lensing analysis of this cluster⁴⁴. We improve the previous lens model with new lensing constraints, including three new spectroscopic redshifts that we measured from the MUSE data. We obtain a spectroscopic redshift for the radial arc S7a/S7b in Sharon et al. (2012), $z_{\text{spec}} = 2.82624$. We identify two new sets of lensed galaxies, at $z_{\text{spec}} = 2.7$ and $z_{\text{spec}} = 5.2$. Including more spectroscopic redshift constraints substantially reduces the lens model uncertainties and improves the accuracy^{44,45}. The lens model is computed using the public software `Lenstool`⁴⁶, which uses a Markov Chain Monte Carlo (MCMC) process to explore the parameter space. The lens model results in a computed projected mass density distribution in the lens plane, magnification maps for any given redshift, deflection fields, and their uncertainties. The deflection matrices are calculated using the lens equation, $\vec{\beta} = \vec{\theta} - d_{ls}/d_s\vec{\alpha}(\vec{\theta})$, where $\vec{\beta}$ is the source position at z_{source} , $\vec{\theta}$ is the observed position, d_{ls} and d_s are the distances from the lens to the source and from the observer to the source, respectively, and $\vec{\alpha}(\vec{\theta})$ is the deflection angle at the observed position. We note that any plane behind the lens can be considered as source plane, and this equation applies as well to the absorber plane.

To assess the completeness of our search for [O II] in emission, we scanned the magnification map near Mg II looking for regions with much lower magnification than on top of G1 and G2. We found none, indicating that these galaxies are not sitting on particularly highly-magnified regions; consequently we can be confident that our absorber candidates are robust and no other galaxies (of similar brightness but non-magnified) got missed from our search.

7 Spatial resolution and impact parameters

We use the deflection matrices to de-lens the coordinates of our binned spaxels into the absorber plane and to calculate impact parameters. Extended Data Figure 3 shows a de-lensed image of the arc projected against the image plane. Due to the inhomogeneous lensing deflection, when the spaxels are traced from the image plane to the absorber plane the shape of the binned spaxels changes in the absorber plane, although there is no overlap between them. Assuming the light rays do not intercept each other after being absorbed, our signal should probe independent areas of the absorber. We discuss below on the unequal spaxel areas.

From Extended Data Figure 3 it also becomes evident that although the angular resolution is constant across the image plane, the actual spatial resolution—defined in the absorber plane—is not. To define an ad-hoc ‘spatial resolution’ we simply take the square root of the area of each de-lensed spaxel. We find that this number ranges from ≈ 4 kpc at the East side of the arc, to ≈ 2 kpc at the western side.

To calculate impact parameters we multiply the de-lensed angular separations between spaxels and G1 by the scale at $z = 0.98$ given by the adopted cosmology, i.e., $7.97 \text{ kpc}''$. From a large set of MCMC realizations, we estimate the statistical 1σ uncertainty associated with the angular separations to be $\lesssim 2\%$. Including model systematics⁴⁵, impact parameters should be precise at the $\lesssim 5\%$ level for the assumed cosmology.

8 Partial covering

The background source is likely to be more extended than the typical size of the absorbing clouds, leading to possible partial covering⁴⁷. To test this effect on our signal we performed a second run of automatic Mg II fits on a 8×8 spaxel map. Extended Data Figure 4 shows the cumulative distributions of W_0 and v for the 4×4 and 8×8 binnings. The stronger binning indeed skews the W_0 distribution to lower values. This is probably due to averaging arc light without Mg II absorption; although given the arc geometry, at this spaxel size, $1.6''$, we expect also some sky contamination (not so in the 4×4 binning). Conversely, *the velocity distribution remains unaffected*. We conclude that (a) the chosen 4×4 binning is our best option above the seeing limitation; (b) we cannot exclude a level of partial covering in our W_0 sample, although such an effect is not affecting the absorption velocities.

Particularly relevant to interpreting our results, the physical areas covered by the binned spaxels are unequal in the absorber plane (Extended Data Figure 3). These areas are of the order of 10 kpc^2 , i.e., at least 10^7 times larger than those probed by the $\lesssim 1\text{-pc}$ quasar beams. Clearly, our arc measurements sample an *average* signal at each position. Therefore, measurements at different positions are comparable with each other and, to a great extent, also *independent* of the spaxel area. The only effect of having uneven areas in the absorber plane should be on the intrinsic scatter of each measurement, with smaller spaxels having more scatter. Obviously one cannot measure this intrinsic scatter, but we consider its effect negligible given that the goal is to make a comparison with measurements obtained along the much narrower quasar beams.

9 Gas covering fractions

To calculate gas covering fractions we compute the fraction of positions having positive detections above a given W_0 cutoff, W_{cut} , in a given impact parameter (D) range. Non-detections are accounted for by considering only (2σ) upper limits below W_{cut} . We select W_{cut} and ranges of D to enable comparisons with two quasar-absorber statistics.

To compare with the survey presented by Chen and collaborators² we assume an average

galaxy magnitude $\langle M_B \rangle = -19.0$ and use $W_{\text{cut}} = 0.5 \text{ \AA}$. We find covering fractions of 100% (2/2; in the range $16 < D < 20 \text{ kpc}$), 80% (4/5; $20 < D < 25 \text{ kpc}$), and 38% (6/16; $25 < D < 39 \text{ kpc}$). The quasar statistics for low-luminosity galaxies gives² 60%, 20% and 0%, respectively for the three D ranges. These figures suggest that the intervening gas covering fraction is larger towards this arc than towards the quasars in that sample.

On the other hand, to compare with the survey presented by Nielsen and collaborators³ we use two cutoffs: $W_{\text{cut}} = 0.6 \text{ \AA}$ and $W_{\text{cut}} = 1.0 \text{ \AA}$. For $W_{\text{cut}} = 0.6 \text{ \AA}$ we find covering fractions of 67% (6/9; $0 < D < 25 \text{ kpc}$), and 20% (4/20; $25 < D < 50 \text{ kpc}$). The quasar statistics for low-luminosity galaxies ($0.07 < L_B/L_B^* < 0.94$) gives³ 71% and 48%, respectively. For $W_{\text{cut}} = 1.0 \text{ \AA}$ we find covering fractions of 18% (2/11) and 4% (1/26), respectively for the same D ranges. The quasar statistics gives 29% and 24%. Thus, for both W_0 cutoffs, the covering fractions towards the arc are *smaller* than towards the quasars in this sample.

Finally, note that all these comparisons are subject to uncertainties because we do not cover exactly the same published impact-parameter ranges.

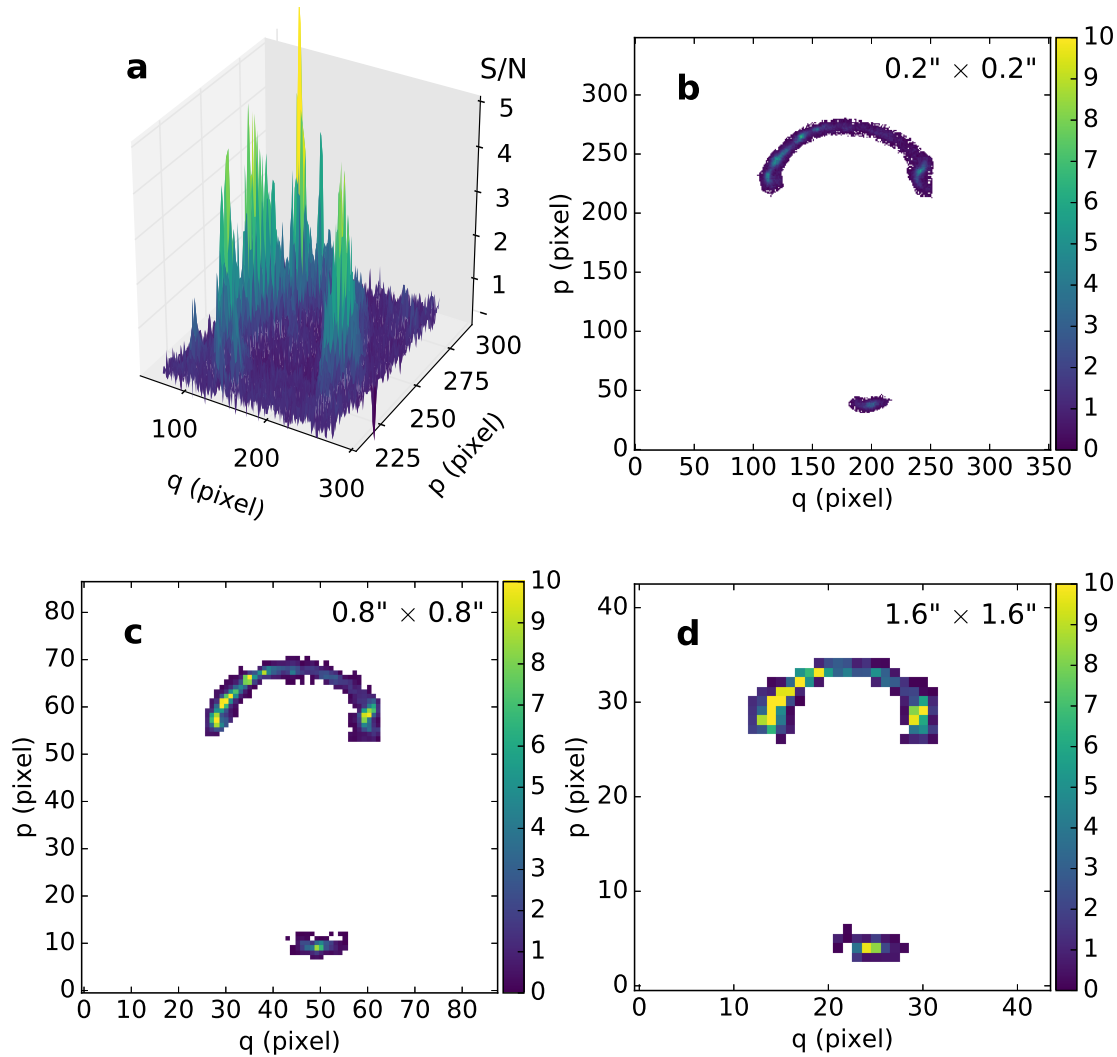
References for Methods

31. Soto, K. T., Lilly, S. J., Bacon, R., Richard, J. & Conseil, S. ZAP - enhanced PCA sky subtraction for integral field spectroscopy. *Mon. Not. R. Astron. Soc.* **458**, 3210–3220 (2016).
32. Bacon, R., Piqueras, L., Conseil, S., Richard, J. & Shepherd, M. MPDAF: MUSE Python Data Analysis Framework. Astrophysics Source Code Library (2016).
33. Robitaille, T. & Bressert, E. APLpy: Astronomical Plotting Library in Python. Astrophysics Source Code Library (2012).
34. Cappellari, M. & Copin, Y. Adaptive spatial binning of integral-field spectroscopic data using Voronoi tessellations. *Mon. Not. R. Astron. Soc.* **342**, 345–354 (2003).
35. Robertson, J. G. Optimal extraction of single-object spectra from observations with two-dimensional detectors. *Publications of the Astronomical Society of the Pacific* **98**, 1220–1231 (1986).
36. Rigby, J. R. *et al.* C III] Emission in Star-forming Galaxies Near and Far. *Astroph. J. Letters* **814**, L6 (2015).
37. Rodríguez Hidalgo, P. *et al.* Evolution of the population of very strong Mg II absorbers. *Mon. Not. R. Astron. Soc.* **427**, 1801–1815 (2012).
38. Bertin, E. & Arnouts, S. SExtractor: Software for source extraction. *Astronomy & Astrophysics Supplement Series* **117**, 393–404 (1996).
39. Coleman, G. D., Wu, C.-C. & Weedman, D. W. Colors and magnitudes predicted for high redshift galaxies. *Astrophys. J. Suppl. Ser.* **43**, 393–416 (1980).

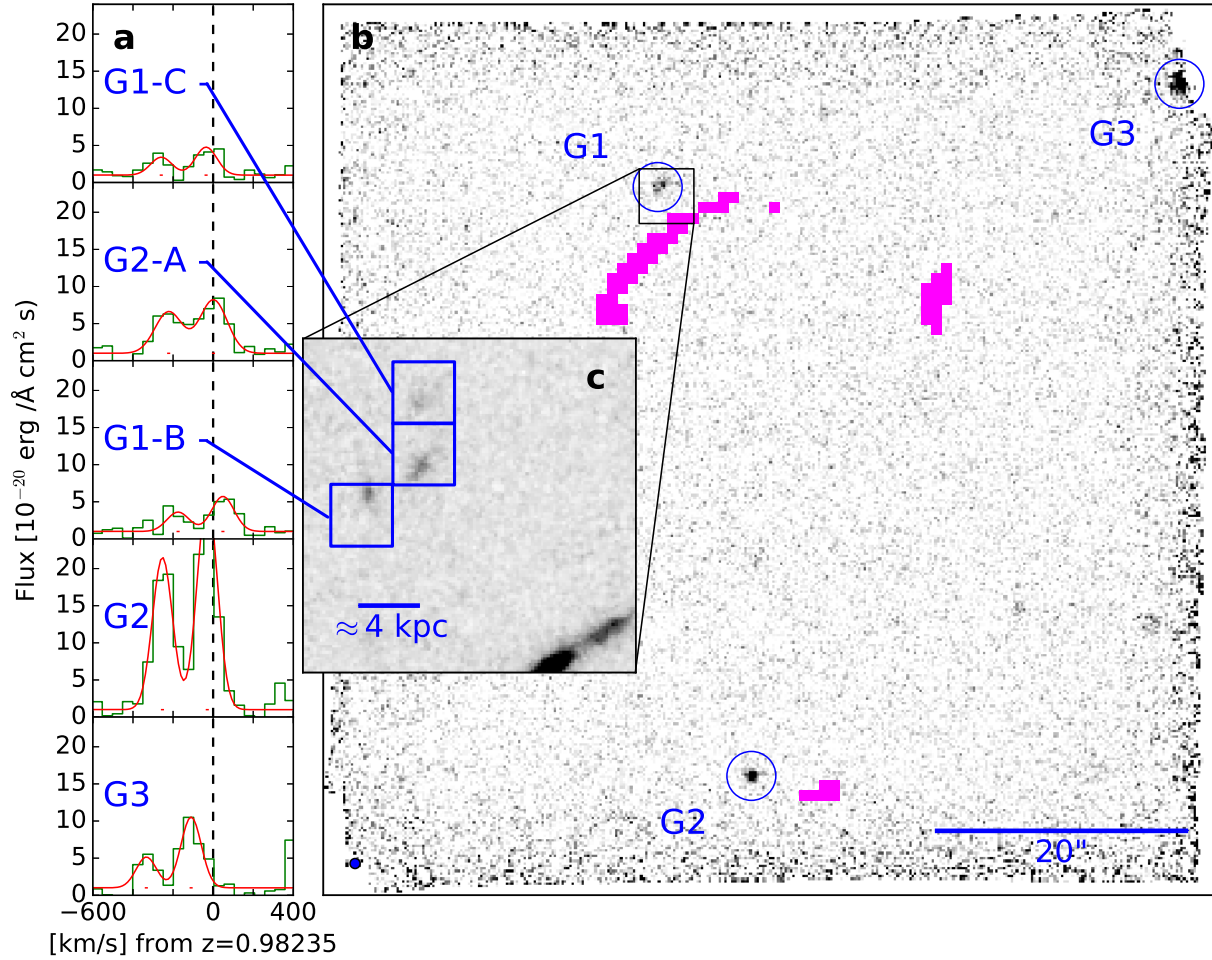
40. Schlegel, D. J., Finkbeiner, D. P. & Davis, M. Maps of Dust Infrared Emission for Use in Estimation of Reddening and Cosmic Microwave Background Radiation Foregrounds. *Astrophys. J.* **500**, 525–553 (1998).
41. Kennicutt, R. C., Jr. Star Formation in Galaxies Along the Hubble Sequence. *Annual Review of Astronomy & Astrophysics* **36**, 189–232 (1998).
42. Moustakas, J. *et al.* PRIMUS: Constraints on Star Formation Quenching and Galaxy Merging, and the Evolution of the Stellar Mass Function from $z = 0-1$. *Astrophys. J.* **767**, 50 (2013).
43. Moster, B. P. *et al.* Constraints on the Relationship between Stellar Mass and Halo Mass at Low and High Redshift. *Astrophys. J.* **710**, 903–923 (2010).
44. Sharon, K. *et al.* Source-plane Reconstruction of the Bright Lensed Galaxy RCSGA 032727-132609. *Astrophys. J.* **746**, 161 (2012).
45. Johnson, T. L. & Sharon, K. The Systematics of Strong Lens Modeling Quantified: The Effects of Constraint Selection and Redshift Information on Magnification, Mass, and Multiple Image Predictability. *Astrophys. J.* **832**, 82 (2016).
46. Jullo, E. *et al.* A Bayesian approach to strong lensing modelling of galaxy clusters. *New Journal of Physics* **9**, 447 (2007).
47. Bergeron, J. & Boisse, P. Extent and structure of intervening absorbers from absorption lines redshifted on quasar emission lines. *ArXiv e-prints* (2017).
48. Willmer, C. N. A. *et al.* The Deep Evolutionary Exploratory Probe 2 Galaxy Redshift Survey: The Galaxy Luminosity Function to $z \sim 1$. *Astrophys. J.* **647**, 853–873 (2006).

Code availability The present analysis is based on custom Python routines, some of which use the MUSE Python Data Analysis Framework³² and the open-source plotting package for Python APLpy³³. We have opted not to make our routines available because these are described in detail in the paper.

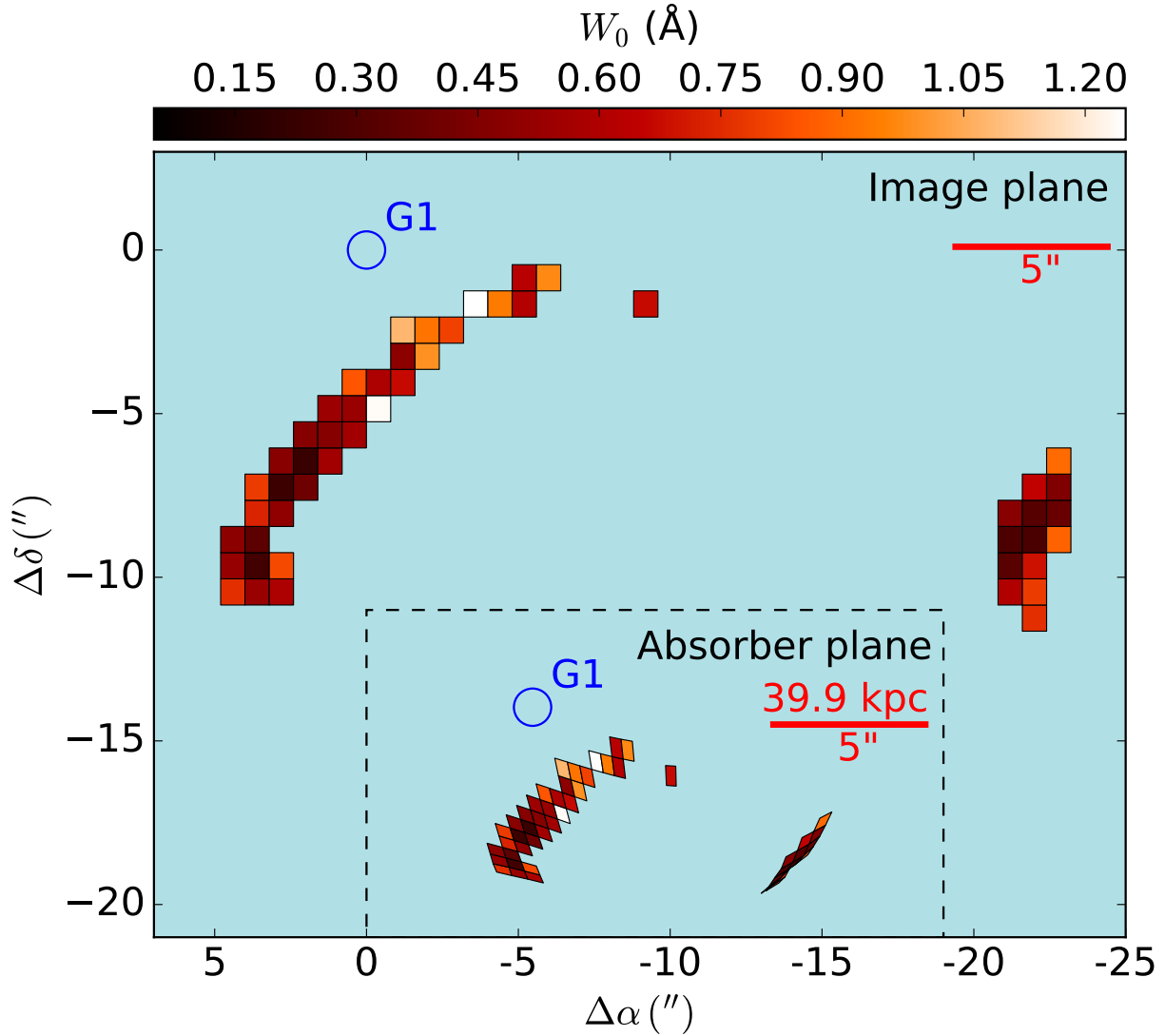
Data availability The observations discussed in this paper were made with European Southern Observatory (ESO) Telescopes at the La Silla Paranal Observatory under programme ID 098A.0459(A). The corresponding data are available on the ESO archive at <http://archive.eso.org/cms.html>.



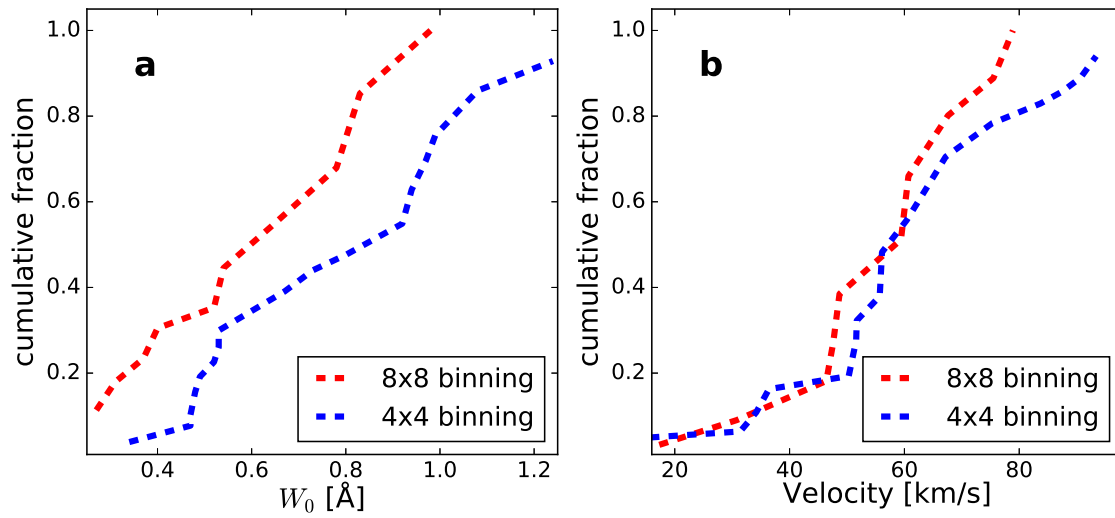
Extended Data Figure 1: **S/N versus binning.** (a): 3-D representation of the S/N at the position of Mg II absorption in the unbinned data. (b)—(d): Same as (a) but in 2-D and for different binnings. The size of each binned spaxel is indicated in arc-seconds. The color scale is the same for all three panels. Note the expected increase in S/N with binning size.



Extended Data Figure 2: **Emission-line galaxies at $z = 0.98$.** **(a):** Gaussian fits to the $[\text{O II}]\lambda\lambda 3726, 3729$ doublets in the MUSE spectra of G1, G2, and G3, the three $[\text{O II}]$ sources found by our systematic search. The MUSE spatial resolution barely resolves G1 into three $[\text{O II}]$ clumps (G1-A, G1-B, and G1-C), which cluster around $z_{\text{G1}} = 0.98235$ and have a velocity dispersion of 35 km s^{-1} . **(b):** MUSE image of RCGSA 032727–132623 centered on $[\text{O II}]$ emission at $z = 0.98$. The magenta squares indicate the binned spaxels used to map the Mg II absorption against the arc. **(c):** *HST*/WFC3 F814W image zooming into the G1 system. The blue squares indicate the MUSE regions used to extract the $[\text{O II}]$ spectra. The scale corresponds to the region close to G1 in the absorber plane.



Extended Data Figure 3: **Projection of absorber plane against image plane.** In the absorber plane (dashed-line rectangle) the spaxel configuration appears shrunk and the de-lensed spatial elements have different shapes and areas across the absorber plane. After de-lensing, the scale in the absorber plane is given by the adopted cosmology, i.e., $5'' = 39.85$ kpc at $z = 0.98$. The impact parameter used in this work is defined as the projected physical distance between a given position and G1 on this plane. For reference, a $5''$ scale bar is shown in the image plane too. Coordinates are in arc-seconds relative to the position of G1 in the image plane.



Extended Data Figure 4: **Effect of partial covering.** **(a):** Cumulative distribution of absorption-strengths for two different binnings. **(b):** Same for velocities.

Extended Data Table 1: Mg II absorption near G1

$\Delta\alpha^a$ (")	$\Delta\delta^a$ (")	D^b [kpc]	W_0^c [Å]	v^d [km s ⁻¹]	S/N ^e
-22.0	-11.2	77.5	< 0.76	...	3.6
4.4	-10.4	40.3	< 0.76	...	3.6
3.6	-10.4	40.5	0.53 ± 0.14	55.7 ± 13.8	8.7
2.8	-10.4	41.3	< 0.59	...	4.6
-21.2	-10.4	76.5	< 0.60	...	4.5
-22.0	-10.4	78.0	< 0.79	...	3.4
4.4	-9.6	38.3	0.52 ± 0.18	15.7 ± 26.3	6.8
3.6	-9.6	38.5	< 0.26	...	10.6
2.8	-9.6	39.2	< 0.82	...	3.3
-21.2	-9.6	77.2	< 0.33	...	8.1
-22.0	-9.6	78.4	< 0.69	...	3.9
4.4	-8.8	36.2	< 0.49	...	5.5
3.6	-8.8	36.2	0.34 ± 0.12	50.3 ± 15.8	8.7
-21.2	-8.8	77.7	< 0.29	...	9.2
-22.0	-8.8	79.5	< 0.28	...	9.8
-22.8	-8.8	81.1	< 0.88	...	3.1
3.6	-8.0	33.8	0.73 ± 0.24	60.4 ± 25.0	5.1
2.8	-8.0	34.3	< 0.50	...	5.4
-21.2	-8.0	77.8	< 0.48	...	5.6
-22.0	-8.0	79.9	< 0.32	...	8.5
-22.8	-8.0	81.8	< 0.38	...	7.1
3.6	-7.2	31.2	< 0.79	...	3.5
2.8	-7.2	31.5	< 0.24	...	11.3
2.0	-7.2	32.6	< 0.40	...	6.8
-22.0	-7.2	80.1	< 0.65	...	4.2
-22.8	-7.2	82.4	< 0.45	...	6.1
2.8	-6.4	28.6	0.48 ± 0.17	34.2 ± 23.5	9.8
2.0	-6.4	29.5	< 0.23	...	12.1
1.2	-6.4	30.7	< 0.56	...	4.8
-22.8	-6.4	82.8	< 0.90	...	3.0
2.0	-5.6	26.3	0.47 ± 0.14	93.4 ± 25.9	7.4
1.2	-5.6	27.4	0.47 ± 0.10	51.7 ± 18.0	10.6
0.4	-5.6	28.9	< 0.56	...	4.9
1.2	-4.8	23.8	< 0.54	...	5.1
0.4	-4.8	25.2	0.53 ± 0.12	63.5 ± 12.3	7.2
-0.4	-4.8	27.1	1.24 ± 0.43	115.4 ± 29.0	3.2
0.4	-4.0	21.4	< 0.85	...	3.2
-0.4	-4.0	23.2	< 0.59	...	4.6
-1.2	-4.0	25.4	0.67 ± 0.26	83.7 ± 16.1	3.2
-1.2	-3.2	21.3	0.49 ± 0.11	75.3 ± 9.9	7.9
-2.0	-3.2	23.8	0.99 ± 0.15	90.7 ± 9.7	8.3
-1.2	-2.4	17.1	1.08 ± 0.19	87.5 ± 12.6	7.8
-2.0	-2.4	19.7	0.92 ± 0.11	51.6 ± 7.3	11.0
-2.8	-2.4	22.4	0.8 ± 0.24	31.4 ± 19.0	5.2
-3.6	-1.6	21.7	1.42 ± 0.20	36.4 ± 11.3	5.0
-4.4	-1.6	24.7	0.94 ± 0.14	56.1 ± 9.2	9.0
-5.2	-1.6	27.3	< 0.61	...	4.5
-9.2	-1.6	40.6	< 0.67	...	4.1
-5.2	-0.8	24.5	< 0.63	...	4.3
-6.0	-0.8	27.6	0.97 ± 0.26	67.2 ± 17.5	3.4

^aArc-position angular separation to G1 in the image plane; ^bProjected physical separation to G1 in the absorber plane; ^cMg II λ 2796 absorption-strength (with 1σ error) or 2σ upper limit; ^dVelocity relative to $z_{G1} = 0.98235$; ^eSignal-to-noise ratio to the blue of Mg II

Extended Data Table 2: Upper limits on Mg II absorption near G2

$\Delta\alpha^a$	$\Delta\delta^a$	D^b	W_0^c	v^d	S/N ^e
($''$)	($''$)	[kpc]	[\AA]	[km s^{-1}]	
-4.2	-1.6	22.0	< 0.81	...	3.4
-5.0	-1.6	25.2	< 0.70	...	3.9
-5.8	-1.6	28.9	< 0.32	...	8.6
-6.6	-1.6	32.5	< 0.41	...	6.7
-5.8	-0.8	27.1	< 0.79	...	3.4
-6.6	-0.8	30.9	< 0.60	...	4.5

^aArc-position angular separation to G2 in the image plane; ^bProjected physical separation to G2 in the absorber plane; ^cMg II λ 2796 absorption-strength 2σ upper limit; ^dVelocity relative to $z_{\text{G1}} = 0.98235$; ^eSignal-to-noise ratio to the blue of Mg II

Extended Data Table 3: Absorption by Fe II and Mg I near G1

$\Delta\alpha$ (")	$\Delta\delta$ (")	D [kpc]	W_0^{2796} [Å]	W_0^{2382} [Å]	W_0^{2852} [Å]
-2.0	-3.2	23.8	0.99 ± 0.15	0.72 ± 0.22	< 0.35
-1.2	-2.4	17.1	1.08 ± 0.19	0.59 ± 0.21	0.44 ± 0.15
-4.4	-1.6	24.7	0.94 ± 0.14	0.62 ± 0.19	< 0.31

Extended Data Table 4: Galaxy properties

ID	RA	DEC	z	v	Δv_{FWHM}	m_{F814W}	$B - I$
	[deg]	[deg]		[km s ⁻¹]	[km s ⁻¹]	(AB)	
(1)	(2)	(3)	(4)	(5)	(6)	(7)	(8)
<i>G1-A</i>	51.867229	-13.434300	0.98236	+1.8 ± 7.0	138.0 ± 10.4	24.30 ± 0.03	0.68 ± 0.03
<i>G1-B</i>	51.867420	-13.434390	0.98267	+48.8 ± 12.0	97.9 ± 18.4	24.64 ± 0.04	0.53 ± 0.04
<i>G1-C</i>	51.867229	-13.434060	0.98212	-35.2 ± 12.5	92.5 ± 17.9	24.85 ± 0.05	0.72 ± 0.05
<i>G2</i>	51.865139	-13.447130	0.98216	-29.2 ± 1.7	81.0 ± 2.8	24.27 ± 0.03	0.06 ± 0.03
<i>G3</i>	51.855511	-13.431970	0.98162	-109.8 ± 12.2	86.9 ± 17.4	23.99 ± 0.02	0.30 ± 0.02
ID	M_B	L/L^*	$\log M_*/M_\odot$	f_{OII}	SFR	μ	R_{vir}
	(9)	(10)	(11)	[erg cm ⁻² s ⁻¹]	[M _⊙ yr ⁻¹]	(14)	[kpc]
	(9)	(10)	(11)	(12)	(13)	(14)	(15)
<i>G1-A</i>	-18.37	0.05	9.5	$8.7 \cdot 10^{-18}$	0.23	2.6	92
<i>G1-B</i>	-17.92	0.03	9.1	$4.0 \cdot 10^{-18}$	0.11	2.7	79
<i>G1-C</i>	-17.81	0.03	9.1	$3.3 \cdot 10^{-18}$	0.09	2.5	79
<i>G2</i>	-18.86	0.08	9.0	$2.4 \cdot 10^{-17}$	0.85	2.0	73
<i>G3</i>	-19.08	0.10	9.4	$6.9 \cdot 10^{-18}$	0.28	1.7	85

Columns.— (1)–(3) Galaxy identification and coordinates; (4) redshift; (5) velocity relative to $z_{\text{G1}}=0.98235$; (6) deconvolved [O II] line width; (7) apparent magnitude; (8) rest-frame color; (9) absolute magnitude; (10) rest-frame B -band luminosity in terms of L^* at $z = 0.98^{48}$; (11) stellar mass (from SED fitting); (12) [O II] emission line flux (13) star formation rate (from emission line flux); (14) magnification (subject to $\approx 5\%$ uncertainties). Magnification was used to correct quantities (9)–(13); (15) virial radius.